

Crustal structure in the middle-southern segments of the Tanlu Fault Zone and adjacent regions constrained by multifrequency receiver function and surface wave data



Zigen Wei^a, Risheng Chu^{a,*}, Ling Chen^{b,c,d}, Shanshan Wu^e

^a State Key Laboratory of Geodesy and Earth's Dynamics, Innovation Academy for Precision Measurement Science and Technology, Chinese Academy of Sciences, Wuhan 430077, China

^b State Key Laboratory of Lithospheric Evolution, Institute of Geology and Geophysics, Chinese Academy of Sciences, Beijing 100029, China

^c University of Chinese Academy of Sciences, Beijing 100049, China

^d CAS Center for Excellence in Tibetan Plateau Earth Sciences, Beijing 100101, China

^e Shanghai Earthquake Agency, Shanghai 200062, China

ARTICLE INFO

Keywords:

Tanlu Fault Zone
Joint inversion of receiver function and surface wave dispersion
Tancheng Ms 8.5 earthquake
N-S regional differences
Vertically alternating high- and low-velocity layers

ABSTRACT

We successively adopt H-k stacking of receiver functions (RFs) and joint inversion of RF and surface wave dispersion with Gaussian factors of 1.0, 2.0 and 3.0 to invert the crustal thickness (H), average V_p/V_s ratio (k) and S-wave velocity beneath 146 broadband seismic stations in the middle-southern segments of the Tanlu Fault Zone (TLFZ) and adjacent regions. These observations, together with previous geologic and geophysical studies, are further used to investigate Phanerozoic tectonic evolution in the study region and the seismogenic environment of the Tancheng Ms 8.5 earthquake. Our results show that the Moho depth and k generally range from 25 to 38 km and 1.65–1.95, respectively. The study region is roughly divided into three parts with different crustal structures from north to south, based on the Cretaceous Tiefogou fault and Triassic Lu'an fault and their extensional profiles, which may reflect different responses to the westward subduction of the Paleo-Pacific and Pacific Plates in the Mesozoic-Cenozoic. In addition to the observed uplifted Moho, high k and vertically alternating high-/low-velocity layers, lateral variations in S-wave velocity and junctions of multiple faults are imaged beneath the Tancheng earthquake zone, which may also contribute to the occurrence of strong earthquakes.

1. Introduction

The Tanlu Fault Zone (TLFZ), which crosses the Dabie Orogen in North China and Northeast China from south to north in roughly the NNE direction (Fig. 1), is the largest active fault zone in eastern China (Deng et al., 2003). The formation and evolution of the TLFZ are related to the Triassic collision between the North China Craton and South China and to the westward subduction of the Paleo-Pacific Plate/Pacific Plate beneath the Eurasia Plate since the Cretaceous, resulting in large-scale left-lateral translation of the Qinling-Dabie Orogen and the northern boundary of the North China Craton (Zhu et al., 2018b). In addition, strong earthquakes often occur in the TLFZ because of the abundant distribution of active faults. For example, the Tancheng earthquake occurred in 1668 ($M_s = 8.5$), causing many casualties and much loss of property (Li et al., 2019). Therefore, the study of deep structures beneath the TLFZ and adjacent regions can provide

important constraints for the tectonic evolution of eastern China and seismogenic mechanisms of strong earthquakes.

Increasing numbers of studies on the deep structure beneath the TLFZ have been performed using multiple geophysical methods. The E-W and regional differences in crustal structure beneath the TLFZ and adjacent regions were found by studying gravity data (Tang et al., 2006), aeromagnetic anomalies (Wang et al., 2018) and magnetotelluric observations (Zhang et al., 2010). Thin lithosphere < 100 km thick and low S-wave velocities in the upper mantle were observed by body wave and surface wave tomography (Xu et al., 2000; Huang et al., 2009; Wu et al., 2018) and receiver function imaging (Chen et al., 2006). Regional differences in P-wave and S-wave velocities beneath the TLFZ and surroundings were imaged by deep seismic sounding data (Li et al., 2006; Duan et al., 2016) and ambient noise tomography (Shen et al., 2016; Meng et al., 2019). The above studies have provided some valuable information on deep structures in the study region. However,

* Corresponding author.

E-mail address: chur@apm.ac.cn (R. Chu).

<https://doi.org/10.1016/j.pepi.2020.106470>

Received 11 October 2019; Received in revised form 3 March 2020; Accepted 4 March 2020

Available online 09 March 2020

0031-9201/ © 2020 Elsevier B.V. All rights reserved.

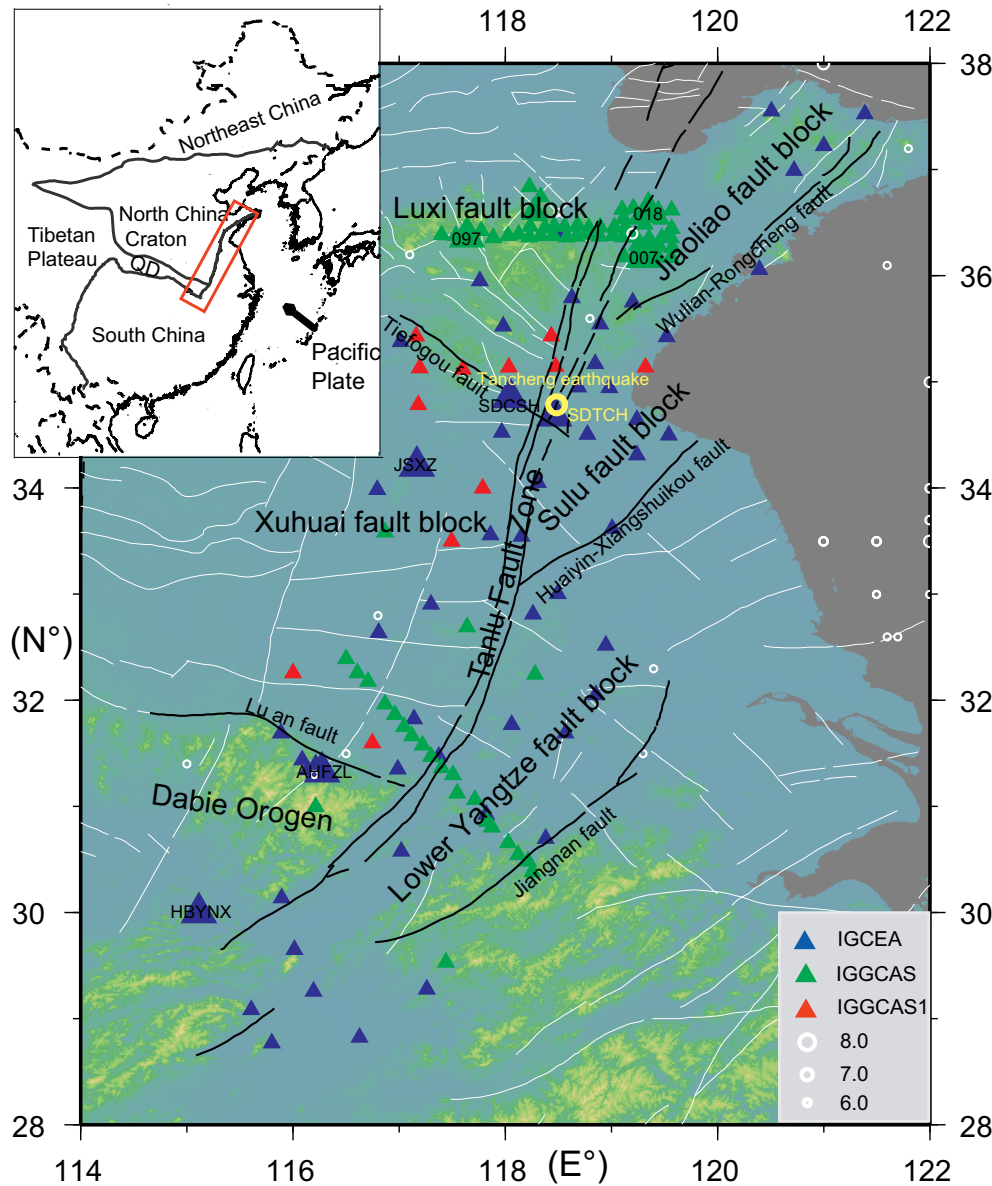


Fig. 1. Geological tectonic setting and distributions of faults (Deng et al., 2003), earthquakes and seismic stations in the study region. The red rectangle in the upper panel shows the Tanlu Fault Zone and surrounding regions. Triangles and lines show the locations of seismic stations and faults (Deng et al., 2003) in the study region. Circles indicate the > 6.0 magnitude earthquakes that occurred from 1500 CE to 2014 (China Earthquake Networks Center). The yellow circle marks the Tancheng Ms 8.5 earthquake that occurred in 1668. QD: Qinling-Dabie Orogen. IGCEA: Institute of Geophysics, China Earthquake Administration; IGGCAS: Institute of Geology and Geophysics, Chinese Academy of Sciences; IGGCAS1: Institute of Geodesy and Geophysics, Chinese Academy of Sciences. (For interpretation of the references to color in this figure legend, the reader is referred to the web version of this article.)

these studies usually have low resolution or are confined to linear profiles, local areas or single crustal features, which is still insufficient for a full understanding of the deep structure and regional differences in the TLFZ and surroundings. More data and multiple parameters are necessary to elucidate the detailed regional differences and lateral variations in crustal structure beneath the TLFZ and adjacent regions.

Crustal thickness, Vp/Vs ratio and velocity are related to the rock composition and stress state, which can provide constraints on continental tectonic evolution (Christensen, 1996; Ji et al., 2009). The simultaneous inversion of receiver functions (RFs) with multiple frequencies can reduce the non-uniqueness of inversion results compared with simple-frequency receiver function inversion (Zhang et al., 2015; Li et al., 2017). In addition, the joint inversion of RF and surface wave dispersion can further reduce the non-uniqueness of RF inversion and increase the resolution of surface wave dispersion inversion (Julià et al., 2000; Hu et al., 2005). In this study, we applied the methods of multifrequency H-k stacking of RFs and joint inversion of multifrequency RF and surface wave dispersion to obtain the Moho depth, Vp/Vs ratio and S-wave velocity in the middle and southern parts of the TLFZ and adjacent regions. Based on the above results, we further studied the crustal structural features and the seismogenic environment of the

Tancheng Ms 8.5 earthquake.

2. Research setting

The TLFZ is the largest NNE-trending fault zone in eastern China. It starts from the eastern part of the Dabie Orogen, passes through North China and Northeast China to the north, and extends into Russia. The TLFZ is ~ 2400 km long in China, with a total length of > 3000 km (Deng et al., 2003; Zhu et al., 2018b). The TLFZ originated from a continental collision between the North China Craton and the Yangtze Craton in the Middle Triassic and then underwent multiphase activity related to the westward subduction of the Pacific Plate (Li, 1994). The active periods and kinematics of the TLFZ can be divided into three main stages: two large-scale left-lateral translations from the Late Triassic to Early Cretaceous, resulting in 550 km of left-lateral displacement for the Dabie-Sulu Orogen and ~ 200 km of left-lateral translation for the northern boundary of the North China Craton; extension from the Cretaceous to Paleogene, resulting in the formation of abundant potentially active fault basins around the TLFZ; and compression and thrusting in the Neogene, resulting in the inversion of red basins surrounding the TLFZ (Yan et al., 2014; Zhu et al., 2018b).

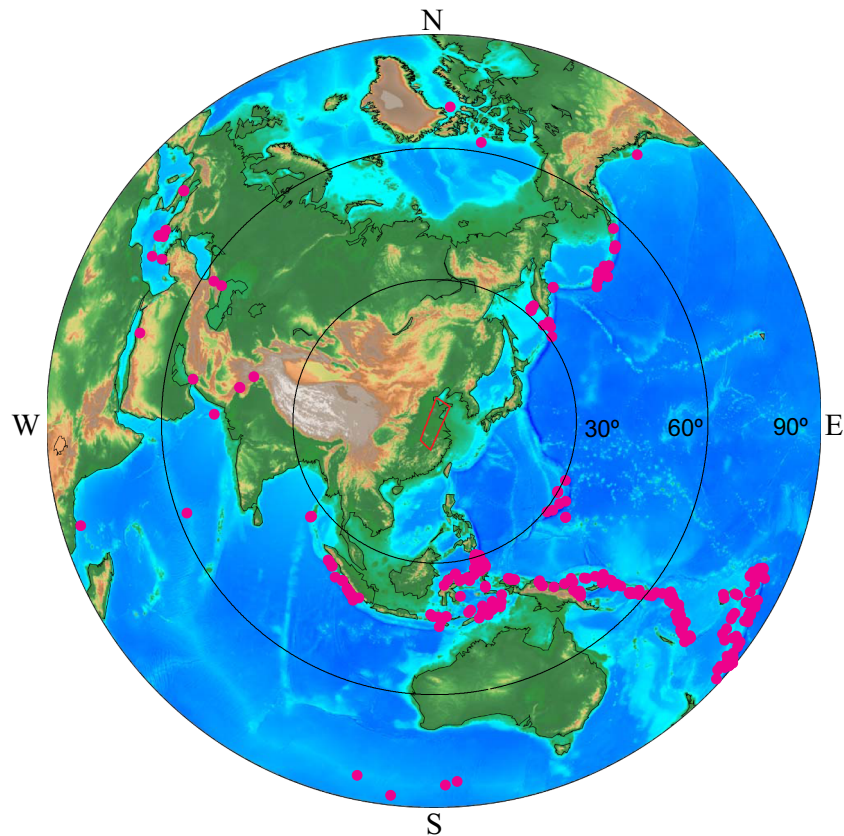


Fig. 2. Teleseismic event distribution (pink solid circles) used for station SDCSH (see the station location in Fig. 1). The red rectangle outlines the study region. (For interpretation of the references to color in this figure legend, the reader is referred to the web version of this article.)

Numerous geologic and geophysical studies have been carried out in the TLFZ in recent years. The TLFZ, with an overall strike of 25° – 40° , is not only a deep fault zone dominated by shear movement for a long time but also a recent active sinistral and thrust fault (Xu et al., 1987; Zhu et al., 2018a). The seismicity is strong in the middle part of the TLFZ based on the analysis of paleoseismicity and seismicity (Zhu et al., 2018b). Based on the observed thinned lithosphere of 60–80 km from the RF poststack migration image (Chen et al., 2006), the TLFZ has been considered a major channel for asthenospheric upwelling during lithospheric thinning in eastern China in the Mesozoic-Cenozoic. By studying the lithospheric S-wave velocity and anisotropic patterns along a near E-W profile in the middle TLFZ and adjacent areas, Zheng et al. (2008) concluded that thermal/chemical erosion may have played a critical role in the reactivation of the North China Craton. A wide zone of linear gradients in the Bouguer gravity anomalies, thicker crust and thinner sediment on the west side were obtained by analyzing Bouguer gravity data in the middle section of the TLFZ and its surroundings (Tang et al., 2006). Regional differences in the Pn velocity and its anisotropy were observed in the middle-southern segments of the TLFZ and adjacent regions (Gu et al., 2016). Resistivity with regional differences and a significantly heterogeneous and high-conductivity layer near the hypocenter area were imaged along an E-W profile crossing the middle TLFZ by analysis of magnetotelluric data (Zhang et al., 2010).

3. Data and method

3.1. Data

We use RFs and phase velocity dispersion curves to image the crustal structure in the study region. RFs are extracted from teleseismic data collected from three different sources (Fig. 1). The two-year data

from 56 permanent stations are from the Data Management Center of China National Seismic Network, Waveform data of China National Seismic Network, Institute of Geophysics, China Earthquake Administration (doi:10.11998/SeisDmc/SN, <http://www.seisdmc.ac.cn>, Zheng et al., 2010). The one-year data from 78 temporary stations with 5–20 km station spacing are from the Seismic Array Laboratory, Institute of Geology and Geophysics, Chinese Academy of Sciences (Zheng et al., 2008; Zhao et al., 2013). The half-year data from 12 temporary stations are from the Institute of Geodesy and Geophysics, Chinese Academy of Sciences. These seismic stations are all equipped with broadband seismometers and cover the study region well. The teleseismic data (Fig. 2) with epicentral distances ranging from 30° to 90° and > 5.5 magnitudes were used to extract the radial P-wave RFs by a time-domain iterative deconvolution method (Herrmann, 2013). For these data, we remove the RFs with unclear P-waves or indistinguishable Ps arrivals by visual inspection and obtain $\sim 15,000$ high-quality RFs for further analysis.

Phase velocity dispersion curves were constructed from two different sources (Fig. 3). Curves with 8–50 s periods from 76 stations in the range of 35° – 38° N were calculated by surface wave tomography with a lateral resolution of 0.5° (Shen et al., 2016). Curves from 70 stations with periods of 5–30 s and 31–50 s in the range of 32° – 35° N were from new ambient noise tomography (Meng et al., 2019) and surface wave tomography (Shen et al., 2016), respectively.

3.2. Methods

3.2.1. Multifrequency H-k stacking method of receiver functions

The time differences between the direct P-wave and the converted Ps/multiple PpPs and PpSs + PsPs phases from the Moho, which are used in the so-called H-k stacking method of RFs, are widely applied to

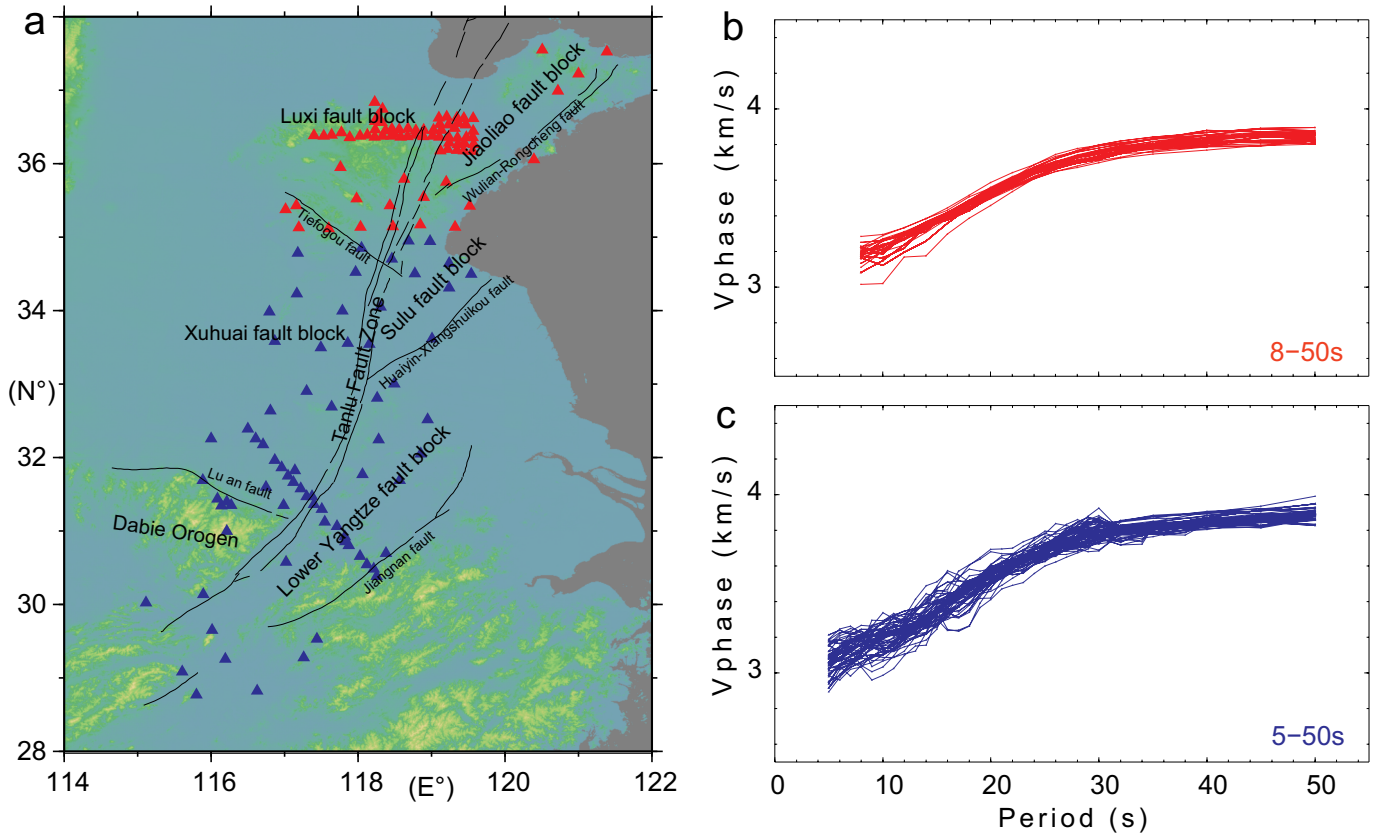


Fig. 3. Distribution of the phase velocity dispersion curves. Red lines in b show the dispersion curves from stations in the range of 35°–38°N in (a). Blue lines in c show the dispersion curves from stations in the range of 32°–35°N in (a). Black lines in (a) show the main faults. (For interpretation of the references to color in this figure legend, the reader is referred to the web version of this article.)

image the crustal thickness (H) and average V_p/V_s ratio (k) beneath each station (Zhu and Kanamori, 2000; He et al., 2014; Wei et al., 2016a). Assuming a 1D single-layer crustal model, the optimal H and k values correspond to the maximum stacking amplitude in this method. In this paper, we calculate H and k using three Gaussian factors of 1.0, 2.0 and 3.0 due to the best balance of the trade-off between resolution preservation and noise suppression in this frequency range. The average values of H and k in different Gaussian factors are used as the last results. In the H - k stacking process, the average crustal P-wave velocity is set to 6.35 km/s according to the seismic exploration results (Li et al., 2006). The weights are set to 0.6, 0.3 and 0.1 for the Ps, PpPs and PpSs + PsPs phases, respectively, based on their progressive decrease in the signal-to-noise ratio. Different weights for these phases do not show noticeable changes to the results. Fig. 4 shows the stacked RF sets with 4° steps in each 8° epicentral distance range for all azimuths and H - k stacking results with different Gaussian factors beneath typical stations. The RFs exhibit consistency between the highest amplitudes and the theoretical arrival times for different phases. The consistency, together with the small uncertainties in the H - k stacking results, suggests the reliability of the crustal thickness and average V_p/V_s ratio.

Recent synthetic tests (Yeck et al., 2013; Yu et al., 2015; Wei et al., 2016b) have found that the traditional H - k stacking results of RFs (Zhu and Kanamori, 2000) significantly deviate from the real values if the Ps phase from the Moho is interfered by phases from sediments, such as the < 1.0 km/s shallow thin layer and > 5 km-thick sediments. The direct P-waves of RFs show the highest amplitudes without delay of arrival times for almost all the stations located in the basin areas, such as the Xuhuai fault block and Lower Yangtze fault block, indicating that the thin layers of ultralow velocity and striking wave impedance are probably absent from the basin areas in the study region (Yeck et al., 2013; Yu et al., 2015). In addition, the Ps phases from the Moho

generally present features of single and sharp peaks in the basin areas, suggesting that the Ps phases are probably not affected by phases from the sediments. The waveforms of the P and Ps phases of RFs are consistent with the sedimentary features, with an overall thickness of < 4.0 km and P-wave velocities of 4.0–4.3 km/s in these basins (Li et al., 2006), and have small effects on single-layer H - k stacking results, as proved by synthetic analysis (Yeck et al., 2013; Wei et al., 2016b). A comparison of H and k values for typical station JSXZ between the traditional single-layer H - k stacking and iterative two-layer H - k stacking considering the sedimentary effect (Yeck et al., 2013) was performed to further study the effect on the H - k stacking results from the sediments in the study region. First, we estimated the sedimentary thickness (h_1) and average V_p/V_s ratio (k_1) using a single-layer H - k stacking method with a Gaussian factor of 7 and P-wave velocity (V_{p1}) in sediment of 4.2 km/s. Then, taking h_1 and k_1 and V_{p1} as input parameters, we estimated the subsediment crustal thickness (h_2) and average V_p/V_s ratio (k_2) using a two-layer H - k stacking method (Yeck et al., 2013) with a Gaussian factor of 2 and P-wave velocity (V_{p2}) in the subsediment crust of 6.4 km/s. Finally, we calculated the average crustal P-wave velocity (V_p) from V_{p1} and V_{p2} and then estimated H and k using the single-layer H - k stacking method with a Gaussian factor of 2. The results (Fig. 5) show that the crustal thickness is 32.7 km by two-layer H - k stacking, which is < 1% thicker than that obtained by single-layer H - k stacking. The average V_p/V_s ratio is 1.76 in the two-layer H - k stacking from the formula $h_1 * k_1 / h + h_2 * k_2 / h$, which is < 2% lower than that obtained by single-layer H - k stacking. Small differences in H and k values between the single-layer and two-layer H - k stacking methods are also observed in the Powder River Basin and Denver Basin in the USA, with sedimentary thicknesses of 2–4 km and P-wave velocities of 3.0–4.0 km/s (Yeck et al., 2013). Based on the waveform features of RFs and the analysis of synthetic (Yeck et al.,

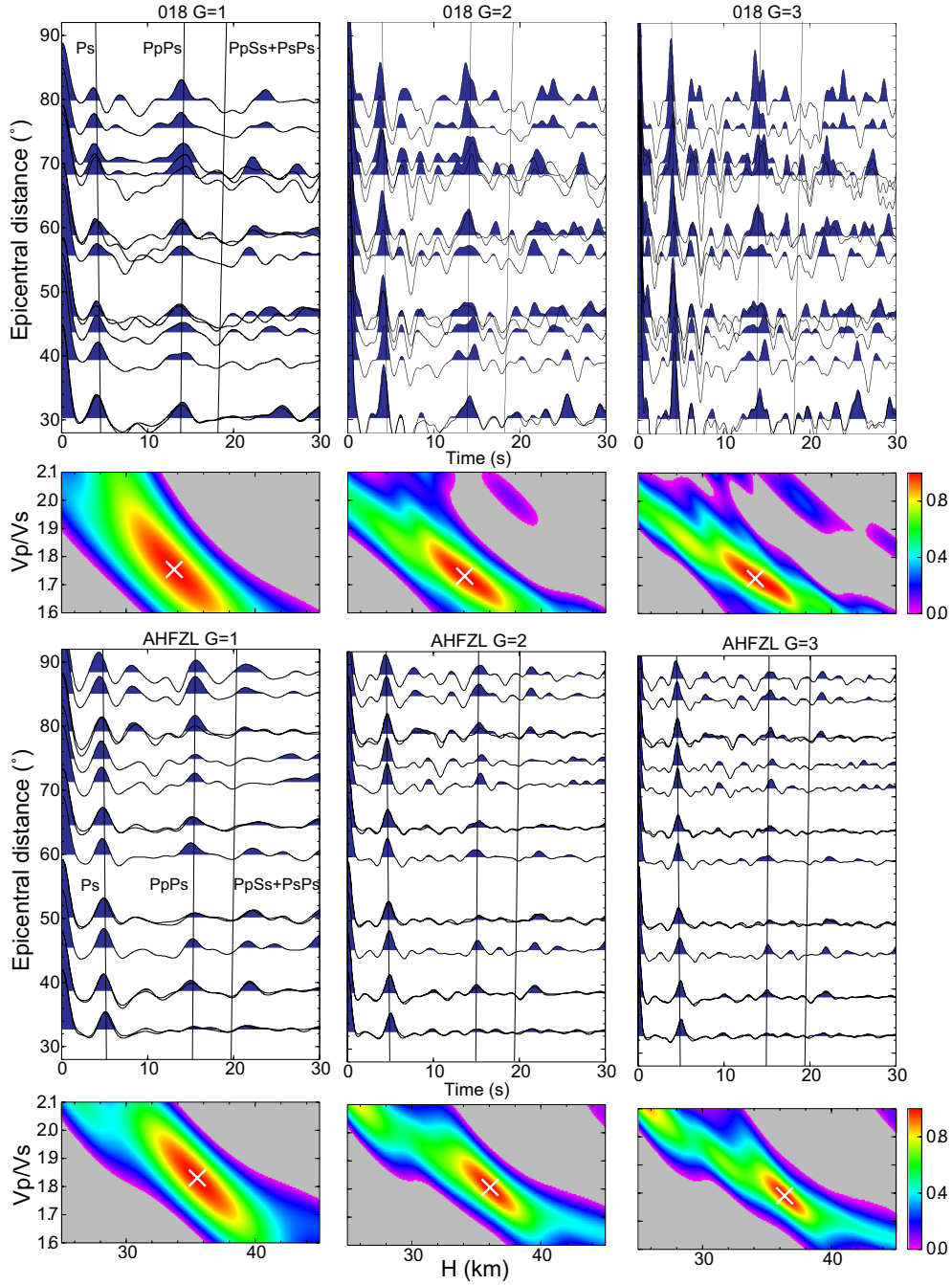


Fig. 4. Receiver functions sorted by epicentral distance with different Gaussian factors (G) of 1.0, 2.0 and 3.0 and corresponding H-k stacking results for typical stations. The black lines denote the theoretical arrival times for the main phases. The colors represent the normalized stacking amplitudes. Crosses show the optimal estimates of H and k . Station locations are shown in Fig. 1.

2013; Wei et al., 2016b) and real data from H-k stacking (Yeck et al., 2013), we believe that the estimated H and k values may represent relatively true structural information about the study region.

3.2.2. Joint inversion of multifrequency receiver function and surface wave dispersion

The joint inversion method of RF and surface wave dispersion (Herrmann, 2013) is used to invert the S-wave velocity in this study by fitting the RFs with multiple Gaussian factors of 1.0, 2.0 and 3.0 and the phase velocity dispersion curves simultaneously. In the inversion process, the initial S-wave velocity for each station comes from the global AK135 model (Kennett et al., 1995); crustal thickness and P-wave velocity are from the H-k stacking results; the first and the second layers

are set to 1 km, while other layers are set to 2 km; and the inversion depth is set to 60 km. We set a 6 km-deep gradient zone around the Moho to decrease the influence of uncertainty in the crustal thickness. Based on the higher lateral resolution of the RFs, we set weight values of 0.7 and 0.3 for the RF and phase velocity dispersion curves. For each Gaussian factor, we fit two RFs in the -5 s– 30 s time window, which are stacked in the 30° – 60° and 60° – 90° epicentral distance ranges for all azimuths. The RFs with fits of $< 65\%$ are deleted to ensure the reliability of the inverted results. The joint inversion results for two typical stations are shown in Fig. 6. The recovered RFs with different Gaussian factors and phase velocity dispersion curves all fit the real data well, suggesting the reliability of the inverted result.

The effects of initial models and data uncertainty on the inversion

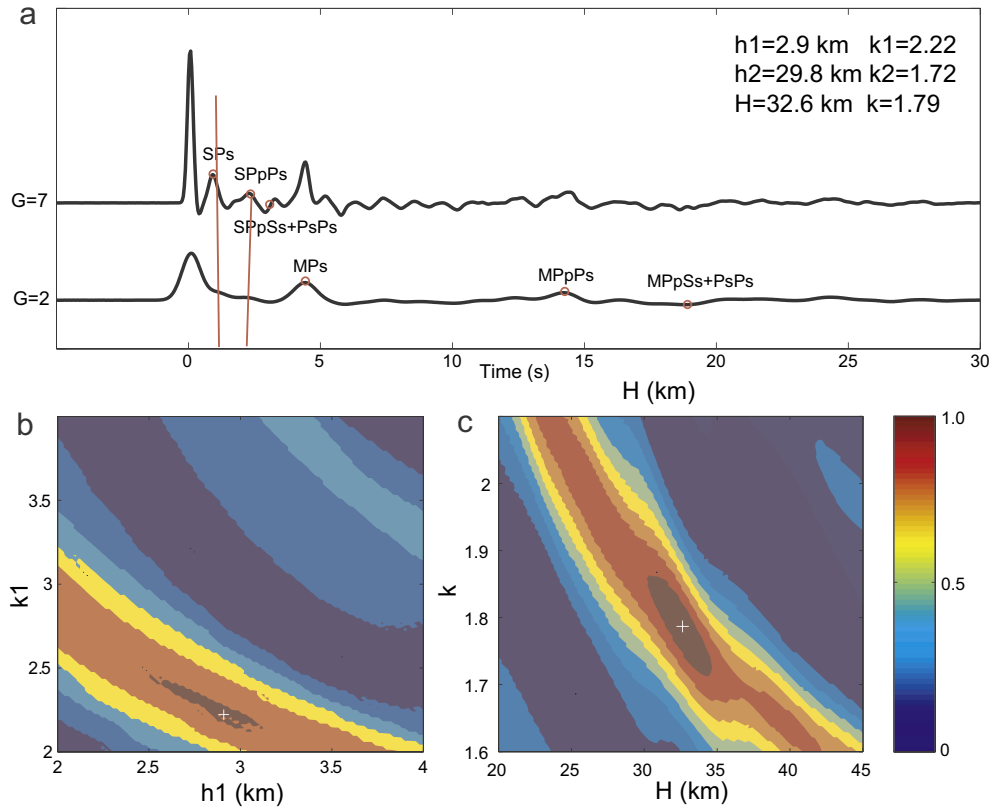


Fig. 5. RF waveforms (a) with Gaussian factors (G) of 2.0 and 7.0 and single-layer H-k stacking results of the sediment and the crust for typical station JSXZ (the station location is shown in Fig. 1). The variables h_1 and k_1 show the sedimentary thickness and average V_p/V_s ratio, respectively. The variables h_2 and k_2 represent the subsediment crustal thickness and average V_p/V_s ratio, respectively. H and k exhibit the crustal thickness and average V_p/V_s ratio. Red circles mark the converted and multiple phases from the sedimentary bottom boundary (SPs, SPpPs and SPpSs+PsPs) and from the Moho (MPs, MPpPs and MPpSs+PsPs). (For interpretation of the references to color in this figure legend, the reader is referred to the web version of this article.)

results are analyzed for the typical stations 007 and 097 shown in Fig. 7, respectively. We set a constant S-wave velocity with $\pm 5\%$ deviations for different initial models (Fig. 7a). The inversion results show that both fitting RFs (Fig. 7b) and phase velocity dispersion curves (Fig. 7c) are almost the same for different initial models with various Gaussian factors. The inverted S-wave velocities (Fig. 7a) are also consistent, with a maximum difference of $\sim 0.1\%$ in different layers for diverse initial models. We perform 100 inversion runs using different data sets for 100 random RFs (Fig. 7e) and 100 random dispersion curves (Fig. 7f) within the $\pm 1\%$ deviations of the observed data, respectively, to study the effects of data uncertainty. The results show that the inverted S-wave velocities have patterns of velocity variation with depth similar to those of the corresponding final inverted model after 100 joint inversions (Fig. 7d). The maximum difference between the final and random models is $\sim 4\%$ at a depth of 8 km. The above tests for the effects from the initial models and data uncertainty indicate that the joint inversion results have strong stability and relative reliability.

4. Results

4.1. Moho depth and V_p/V_s ratio

Fig. 8 shows the average Moho depth and V_p/V_s ratio by H-k stacking of RFs with different Gaussian factors in the study region. The Moho depth (Fig. 8a) and k (Fig. 8b) mainly vary in the ranges of 25–38 km and 1.65–1.95, respectively, and both show strong lateral inhomogeneity and differences in separate blocks. The Moho depth and k exhibit striking E-W differences in some areas on either side of the TLFZ, such as generally thicker crust and lower k in the western Xuhuai fault block compared to the eastern Lower Yangtze fault block. The study region from north to south is roughly divided into three parts with different crustal structures. To the north of the Tiefogou fault and its eastward extension profile, the Moho depth mainly varies around 33 km, and a high k of > 1.85 is mainly distributed along the TLFZ. In the middle part between the Tiefogou and

Lu'an faults and their eastern extension profiles, the Moho depth and k to the east of the TLFZ are generally < 31 km and > 1.85 , respectively, while the Moho depth and k to the west of the TLFZ are overall > 31 km and < 1.8 , respectively. To the south of the Lu'an fault and its eastward extension profile, the Moho depths to the east and to the west of the TLFZ change in the ranges of 28–32 km and 32–38 km, respectively, while k shows no E-W difference around the TLFZ.

4.2. S-wave velocity in the study region

The S-wave velocities imaged by the joint inversion of the multi-frequency RF and phase velocity dispersion curves are shown at different depths in Fig. 9. Similar to the Moho depth and k , the S-wave velocity is also roughly divided into three parts from north to south based on the Tiefogou fault and Lu'an fault and their extensional profiles. At a depth of 2 km (Fig. 9a), the S-wave velocity is generally > 3.1 km/s in the northern and southern parts but generally < 3.1 km/s in the middle part. At a depth of 10 km (Fig. 9b), the S-wave velocity is generally < 3.5 km/s in the northern part, is overall higher (> 3.5 km/s) to the west of the TLFZ than to the east in the middle part, and is higher around the TLFZ in the southern part. At a depth of 18 km (Fig. 9c), the S-wave velocity is overall > 3.5 km/s in the northern part, is generally higher to the west of the TLFZ than to the east (< 3.5 km/s) in the middle part, and is overall lower to the west of the TLFZ than to the east (> 3.5 km/s) in the southern part. At a depth of 26 km (Fig. 9d), the S-wave velocity is overall < 3.7 km/s in the TLFZ and its surroundings. At a depth of 34 km (Fig. 9e), the S-wave velocity is overall < 4.25 km/s in the northern part, is generally > 4.25 km/s in the TLFZ and its surroundings in the middle part, and is overall < 4.2 km/s in the TLFZ and to the west in the southern part. At a depth of 42 km (Fig. 9f), the S-wave velocity is overall < 4.4 km/s and shows strong lateral variations in the northern part, is generally higher to the west of the TLFZ than to the east (< 4.4 km/s) in the middle part, and is generally < 4.4 km/s in the southern part.

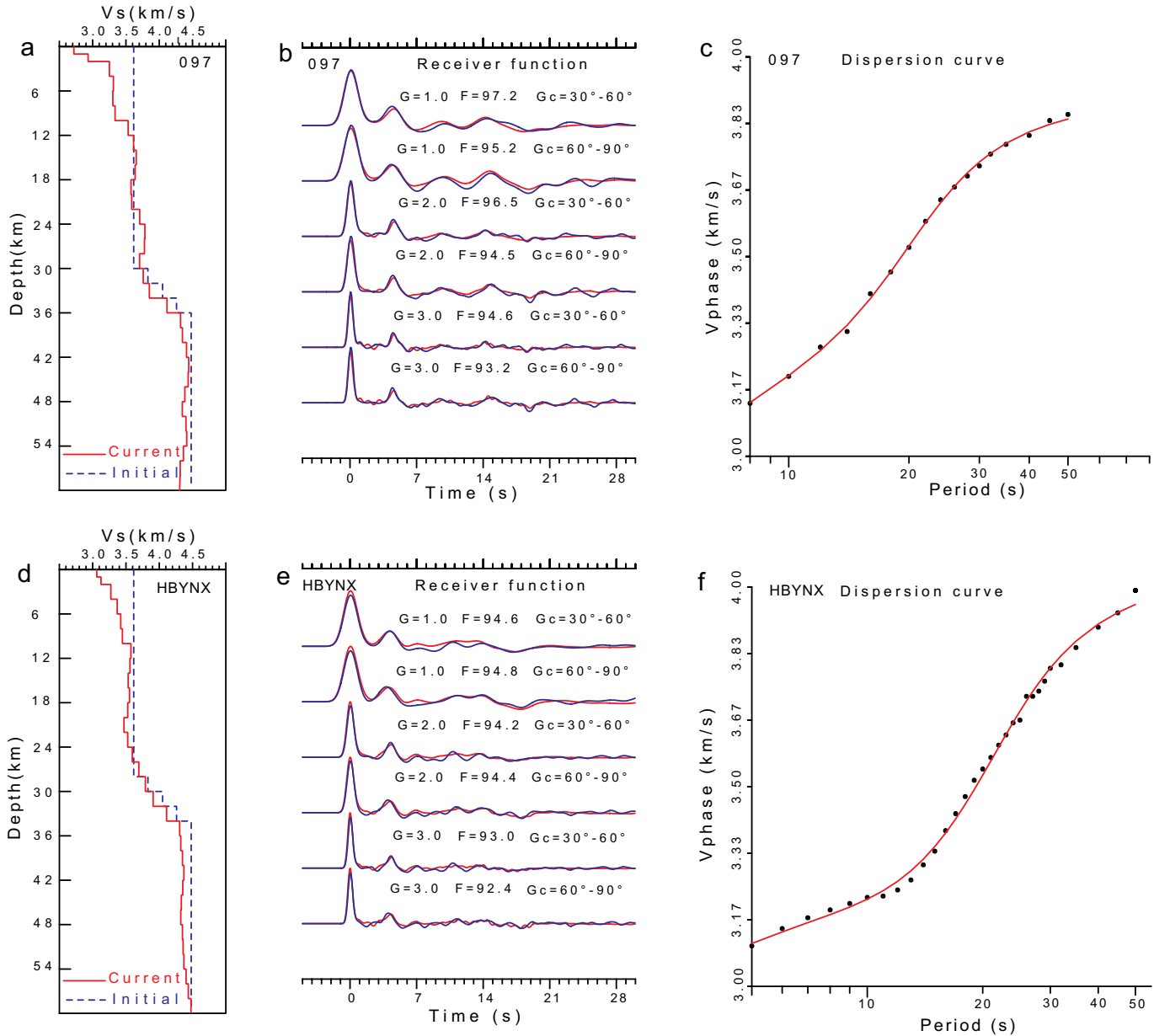


Fig. 6. Schematic diagrams for joint inversion of multifrequency RF and phase velocity dispersion curves for typical stations (see station locations in Fig. 1). Red lines denote the recovered S-wave velocity models (a, d), receiver functions (b, e) and dispersion curves (c, f). G, F and Gc in panels b and e are the Gaussian factor, fitness and epicentral distance, respectively. (For interpretation of the references to color in this figure legend, the reader is referred to the web version of this article.)

5. Discussion

The Moho depth, V_p/V_s ratio and S-wave velocity obtained in this study are consistent with results from single-frequency H-k stacking of RFs (He et al., 2014), RF imaging (Zheng et al., 2008), surface wave tomography (Huang et al., 2009; Zheng et al., 2011), seismic exploration (Li et al., 2006) and other geophysical methods, such as the significant lateral changes and regional differences in the crust. However, new imaging methods and denser data used in this study allow us to observe finer crustal structures and obtain new discoveries in the middle-southern TLFZ and adjacent regions, which are combined with three linear profiles in the following sections.

5.1. Crustal segmentation characteristics beneath the TLFZ

The study region can be divided into three parts, with different crustal structures and topographies, from north to south along the

Cretaceous Tiefogou fault and Triassic Lu'an fault (Deng et al., 2003; Ma, 2002) and their extensional profiles (Figs. 8 and 9). In the northern part dominated by hills, the Moho depth generally varies around 33 km, and high k are mainly found beneath the TLFZ (Fig. 8). The values of the S-wave velocity are roughly consistent on both sides of the TLFZ at different depths (Fig. 9). Lower S-wave velocities extend to a depth of ~20 km beneath the TLFZ, especially in the areas with dense station coverage, where the Moho is uplifted and k is relatively high (Fig. 10b). In the middle part delimited by the Tiefogou fault and Lu'an fault and their extensional profiles, a striking E-W difference in the crust is evident on either side of the TLFZ, although both sides are basins with low elevations. The Moho depth and k are generally thicker and lower, respectively, on the western side of the TLFZ (Fig. 8). The S-wave velocities are lower overall on the eastern side of the TLFZ in the upper-middle crust and uppermost mantle (Figs. 9 and 10c). In the southern part, the Moho depth is greater overall on the western side of the TLFZ accompanied by higher elevations, and k shows lateral variations

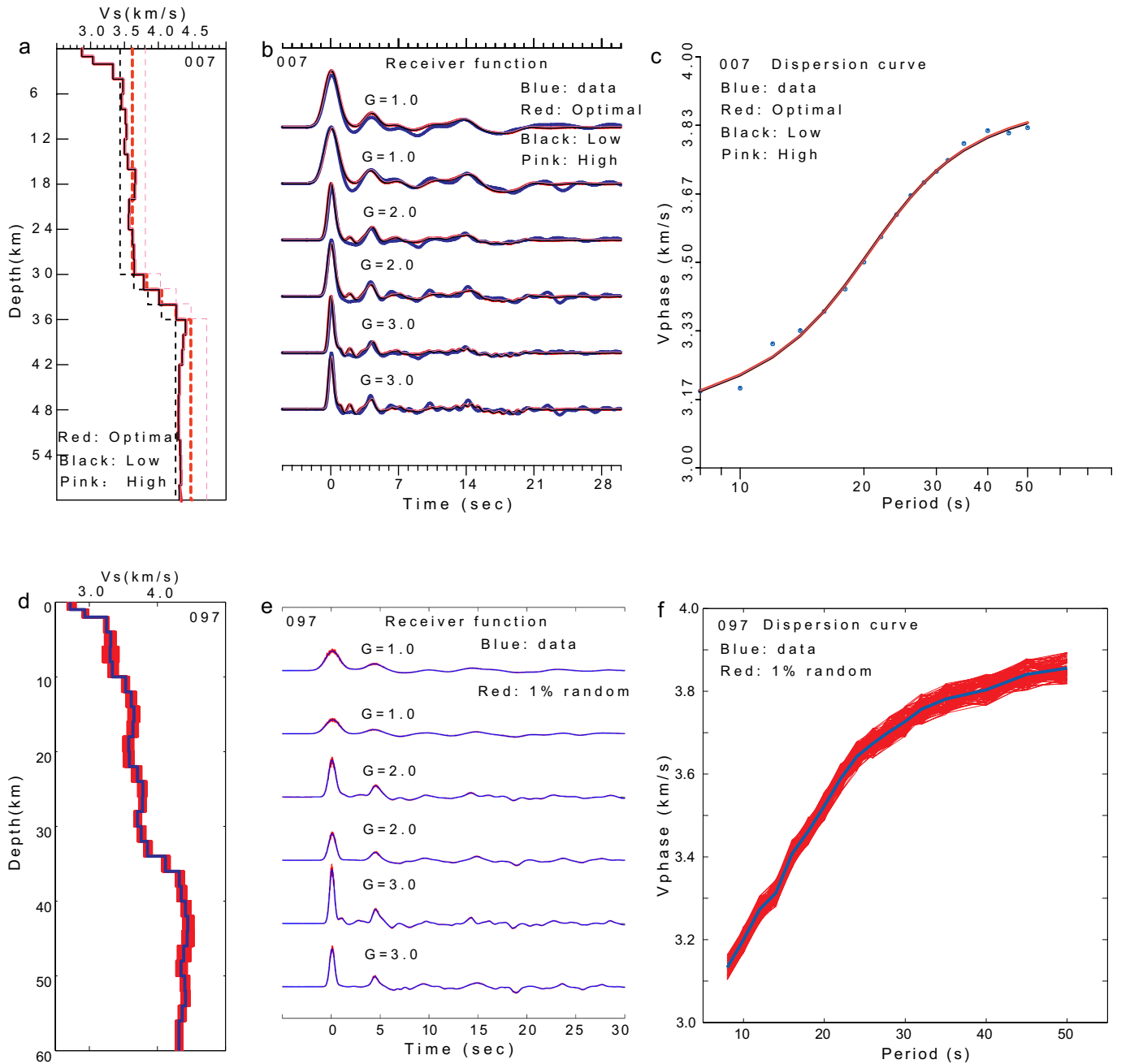


Fig. 7. Effects of initial models and data uncertainty on the inversion results for typical stations 007 and 097. The two initial models (black and pink dashed lines in a) were designed with crustal velocities having $\pm 5\%$ deviations from the optimal initial model (red dashed line in a). b) and c) show the fitting RFs and phase velocity dispersion curves with different Gaussian factors (G), respectively. Red lines show 100 inverted models (d) from different data sets for 100 random RFs (e) and 100 random dispersion curves (f) within the $\pm 1\%$ deviations of the observed data, respectively. The optimal inverted model and real observational data are also plotted with blue lines in d, e, f. (For interpretation of the references to color in this figure legend, the reader is referred to the web version of this article.)

without any obvious E-W difference (Fig. 8). The S-wave velocities show strong lateral variations without striking E-W differences and consistency (Fig. 9).

The N-S differences in the crust within the study region have been observed in previous studies. The crustal S-wave velocity in the southern part is higher than those in the middle and northern parts by surface wave tomography (Huang et al., 2009). The E-W difference in S-wave velocities in the crust has been imaged in the middle part of the

study region by ambient noise tomography (Meng et al., 2019). The Pn wave velocity is the highest on the eastern side of the TLFZ in the middle part of the study region (Gu et al., 2016).

The TLFZ experienced multiple alternations of compressive-torsional translational and extensional activities in the Mesozoic and Cenozoic, which are related to the westward subduction of the Paleo-Pacific Plate and Pacific Plate beneath the Eurasian Plate (Zhu et al., 2018b). The observed features of the N-S segment in this study may

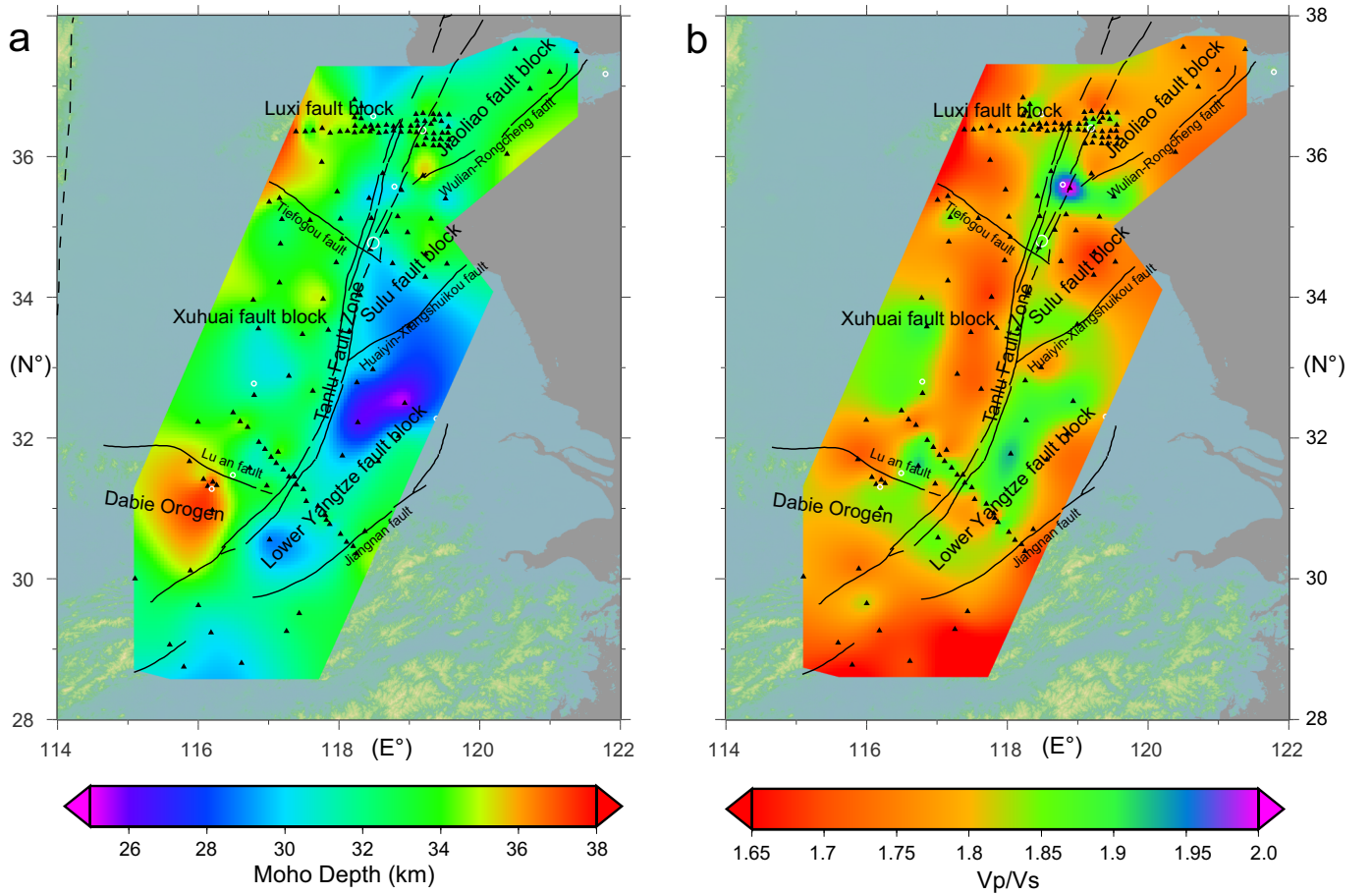


Fig. 8. Average Moho depth (a) and V_p/V_s ratio (b) with different Gaussian factors of 1.0, 2.0 and 3.0. Black lines indicate the main faults. Triangles and circles show the seismic station and earthquake locations, respectively.

reflect different responses of the study region to the Paleo-Pacific Plate and Pacific Plate subduction. The observed lower S-wave velocity in the upper-middle crust and high k mainly limited to the TLFZ in the northern part are consistent with the thinning lithosphere (Chen et al., 2006) and the Cretaceous and Cenozoic volcanic rocks (Fig. 10a) along the TLFZ (Ma, 2002), suggesting that the lithospheric modification in this area may have reached as high as the base of the crust (Zheng et al., 2011) and the crustal structural abnormality may be related to the intrusion of mantle material in Mesozoic-Cenozoic time. A crustal-detachment model was proposed for the collision between the North China Craton and the Yangtze Craton east of the TLFZ based on the observations from aeromagnetic anomalies, surface geology and deep seismic profiles (Li, 1994). According to this model, the lower crust should show similar structural characteristics and the upper crust should show different structural characteristics between the eastern and western sides in the middle part of the TLFZ during the Late Jurassic. In this study, the observed S-wave velocities are similar on both sides in the lower crust, but are lower overall on the eastern side of the TLFZ in the upper crust and uppermost mantle (Figs. 9 and 10c), which is consistent with the crustal-detachment model. Thinner crust, higher k (Fig. 8) and lower S-wave velocity (Figs. 9 and 10) on the eastern side along the TLFZ in the middle part are related to its closer location to the subducting Pacific Plate, which results in stronger extension, intrusion of mantle material and outcrops of Cretaceous and Cenozoic volcanic rocks (Fig. 10a). The complicated crustal structure in the southern part,

as well as the absence of Cenozoic rocks, suggests that this area may be relatively less affected by the Pacific subduction.

5.2. Crustal structure in the source zone of the Tancheng Ms 8.5 earthquake

The Tancheng Ms 8.5 earthquake in 1668, which resulted in the deaths of 50,000 people, produced a surface rupture zone ~230 km long and a maximum horizontal displacement of 7–9 m (Gao et al., 1998). Field work found that the seismic fault of the Tancheng earthquake, with a source depth of ~23 km, was a right-lateral strike-slip thrust fault with a high angle (Wang and Geng, 1996). The vertical movement in the crust for the source zone of the Tancheng earthquake was strong based on exploring the earthquake with gravity and magnetic anomalies and geological data (Liu et al., 1983). The present seismic activity in the middle part of the TLFZ is mainly distributed linearly along the Tancheng earthquake rupture zone and is considered aftershock activity with long and slow attenuation of the Tancheng earthquake (Zhu et al., 2018a).

In this study, a shallower Moho, higher k of > 1.87 (Fig. 8) and a high- to low-velocity transition zone at different depths in the crust (Fig. 9) are observed beneath the Tancheng Ms 8.5 earthquake zone, suggesting that the crust might have been affected by the upwelling of mantle material. For station SDTCH immediately adjacent to the Tancheng earthquake, the S-wave velocity (red line in Fig. 11a) increases roughly from the surface to 3.74 km/s at a depth of 24 km, suddenly

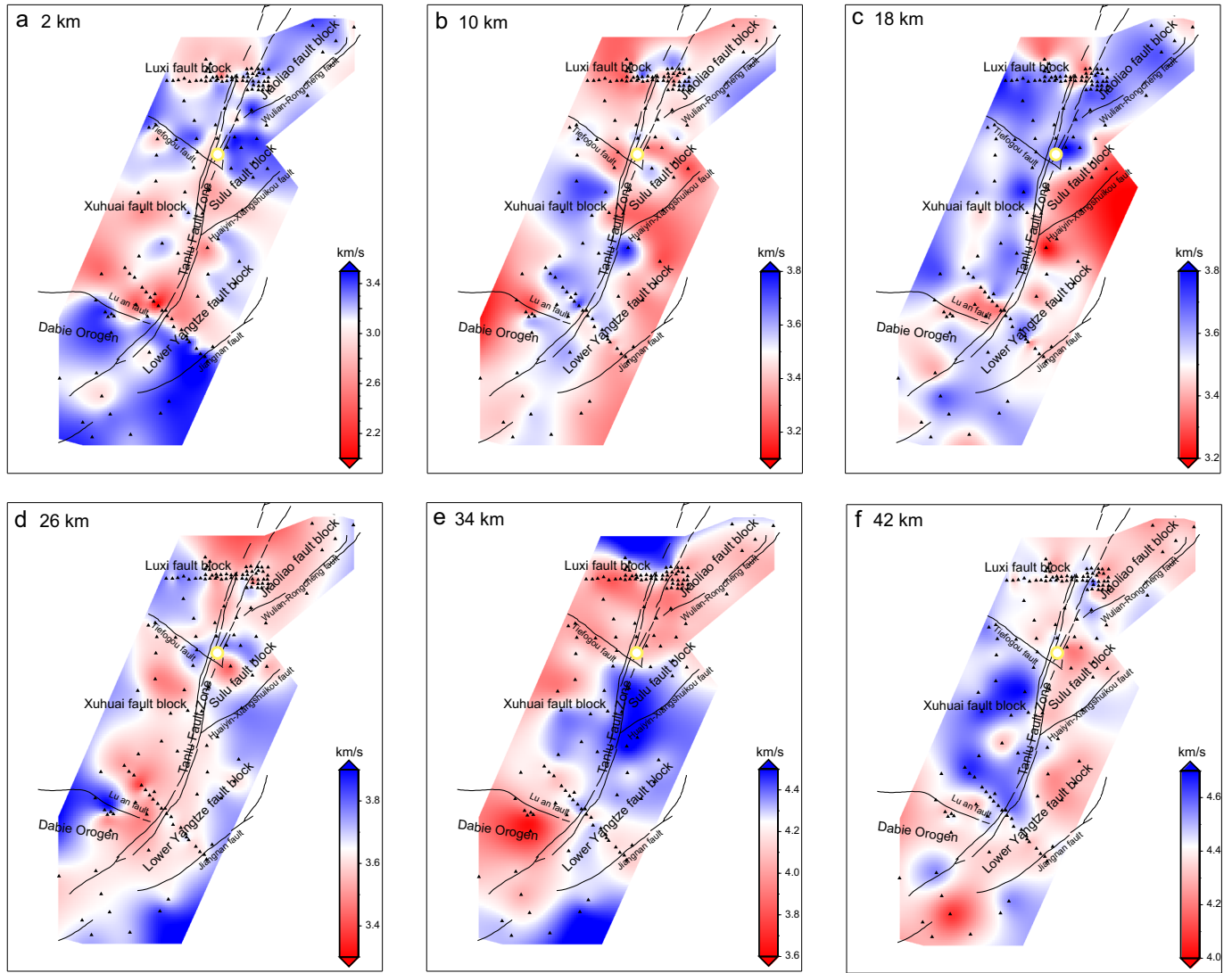


Fig. 9. The S-wave velocity distributions at different depths in the study region. Black lines indicate the main faults. Triangles show the station locations. The yellow circles mark the Tancheng Ms 8.5 earthquake that occurred in 1668. (For interpretation of the references to color in this figure legend, the reader is referred to the web version of this article.)

decreases and remains 3.58 km/s from depths of 24–28 km, and then gradually increases from 28 km to the Moho. The corresponding RFs (red line in Fig. 11c) show a high fitting degree of 90.39% to the real data (black line in Fig. 11c). These observations suggest that the Tancheng earthquake, with a source depth of 23 km, occurred in a high-velocity layer among vertically alternating high- and low-velocity layers. A comparison of different S-wave velocities at depths of 22–30 km based on the last inversion model (Fig. 11a, b) and the corresponding synthetic RFs and real data (Fig. 11c, d) is further analyzed beneath station SDTCH. The results show that the S-wave velocity used in this study (red line in Fig. 11a) has the best fit in terms of both the fitting degree and the PpPs phase between the synthetic RFs and real data, compared to models with no lower velocity at depths of 24–28 km (green lines in Fig. 11a, c), lower velocity at depths of 22–26 km (blue lines in Fig. 11b, d) and lower velocity at depths of 26–30 km (pink lines in Fig. 11b, d). The observed P-wave velocity from deep seismic sounding data beneath the Tancheng earthquake area gradually increases from 6.5 km/s to 6.8 km/s in the depth range of

20–24 km range, decreases rapidly to 6.2 km/s in the depth range of 24–28 km, and then increases to the Moho, which is consistent with the imaged S-wave velocity in this study (Zhang and Tang, 1988). The above observations, together with the ~2 km vertical resolution of RFs assuming an average crustal S-wave velocity of 3.6 km/s and a period of 1 s, show that the lower velocity at depths of 24–28 km may reflect the real structure beneath the Tancheng earthquake zone.

The observed uplifted Moho, high V_p/V_s ratio, and vertically alternating high- and low-velocity layers beneath the Tancheng earthquake zone in our study are consistent with the observed seismogenic environment of strong earthquakes ($M_s \geq 6.5$) occurring in continental China (Teng, 2010), where strong earthquakes were believed to be caused often by vertical material movements of the crust and mantle. In addition, lateral high- and low-velocity variations at different depths and at the junction of two large faults, the TLFZ and the Tiefogou fault, are found beneath the Tancheng earthquake zone. These observations show that, except for the strong vertical movement of deep materials and vertically alternating high- and low-velocity layers, the occurrence

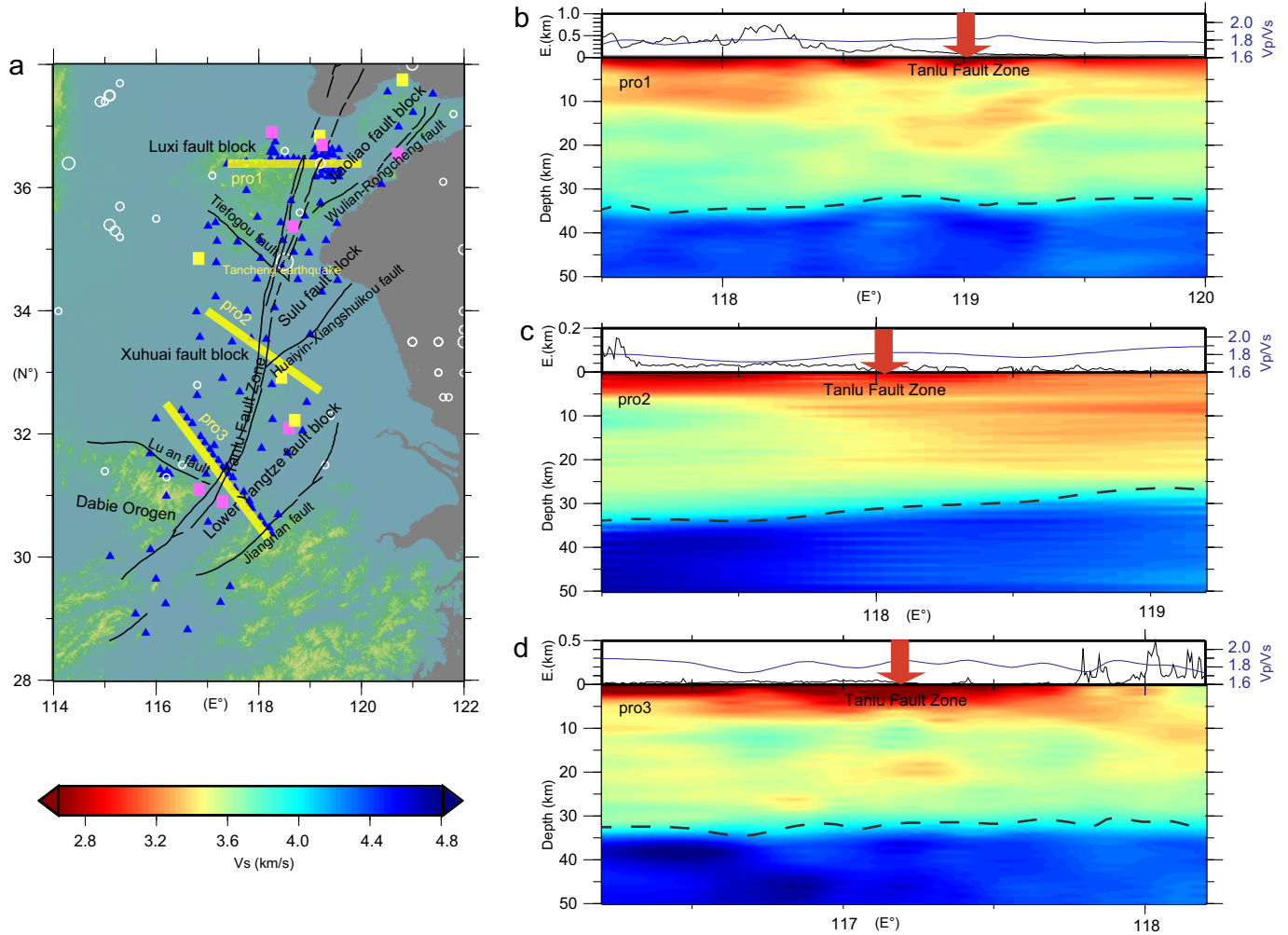


Fig. 10. S-wave velocity, Vp/Vs ratio and elevation (E.) beneath three typical profiles (a). Black lines indicate the main faults. Triangles and circles show the station and earthquake locations, respectively. Pink and yellow rectangles show the locations of Cretaceous and Cenozoic volcanic rocks (Ma, 2002), respectively. Dashed lines (b, c, d) mark the Moho depths beneath the profiles. (For interpretation of the references to color in this figure legend, the reader is referred to the web version of this article.)

of strong earthquakes may be facilitated by lateral variations in velocity and junctions of multiple faults beneath the source zone.

6. Conclusions

We applied the multifrequency H-k stacking of RFs to image the Moho depth and crustal average Vp/Vs ratio beneath the middle-southern segments of the TLFZ and adjacent regions. Referring to the H-k stacking results, we further adopted the joint inversion of the multifrequency RF and surface wave dispersion to obtain the S-wave velocities in the crust and uppermost mantle. These observations, together with previous geophysical and geologic results, were then used to study the crustal structural features and seismogenic environment of the Tancheng Ms 8.5 earthquake.

The Moho depth mainly changes from 25 to 38 km, and k generally varies in the range of 1.65–1.95. The study region is roughly divided into three parts with different crustal structures from north to south based on the Cretaceous Tiefogou fault and the Triassic Lu'an fault and their extensional profiles. In the northern part, the Moho depth mainly

varies around 33 km, and high k and a shallow Moho generally exist along the TLFZ. The S-wave velocity shows small variations at different depths. In the middle part, the Moho depth, k and S-wave velocity in the upper-middle crust are generally thicker, lower and higher, respectively, on the western side of the TLFZ. In the southern part, the Moho depth is greater overall on the western side of the TLFZ, and k and S-wave velocity show lateral variations without obvious E-W differences. The N-S regional differences in the crust may reflect various responses to the westward subduction of the Paleo-Pacific Plate and the Pacific Plate in the Mesozoic and Cenozoic and may also be related to the intrusion of mantle materials.

An uplifted Moho, a high Vp/Vs ratio, and vertically alternating high- and low-velocity layers are observed beneath the Tancheng 8.5 Ms earthquake zone, which is consistent with the seismogenic environment of strong earthquakes occurring in continental China (Teng, 2010). In addition, obvious lateral variations in S-wave velocity and junctions of multiple faults are imaged beneath the Tancheng earthquake zone, which may further contribute to the occurrence of strong earthquakes.

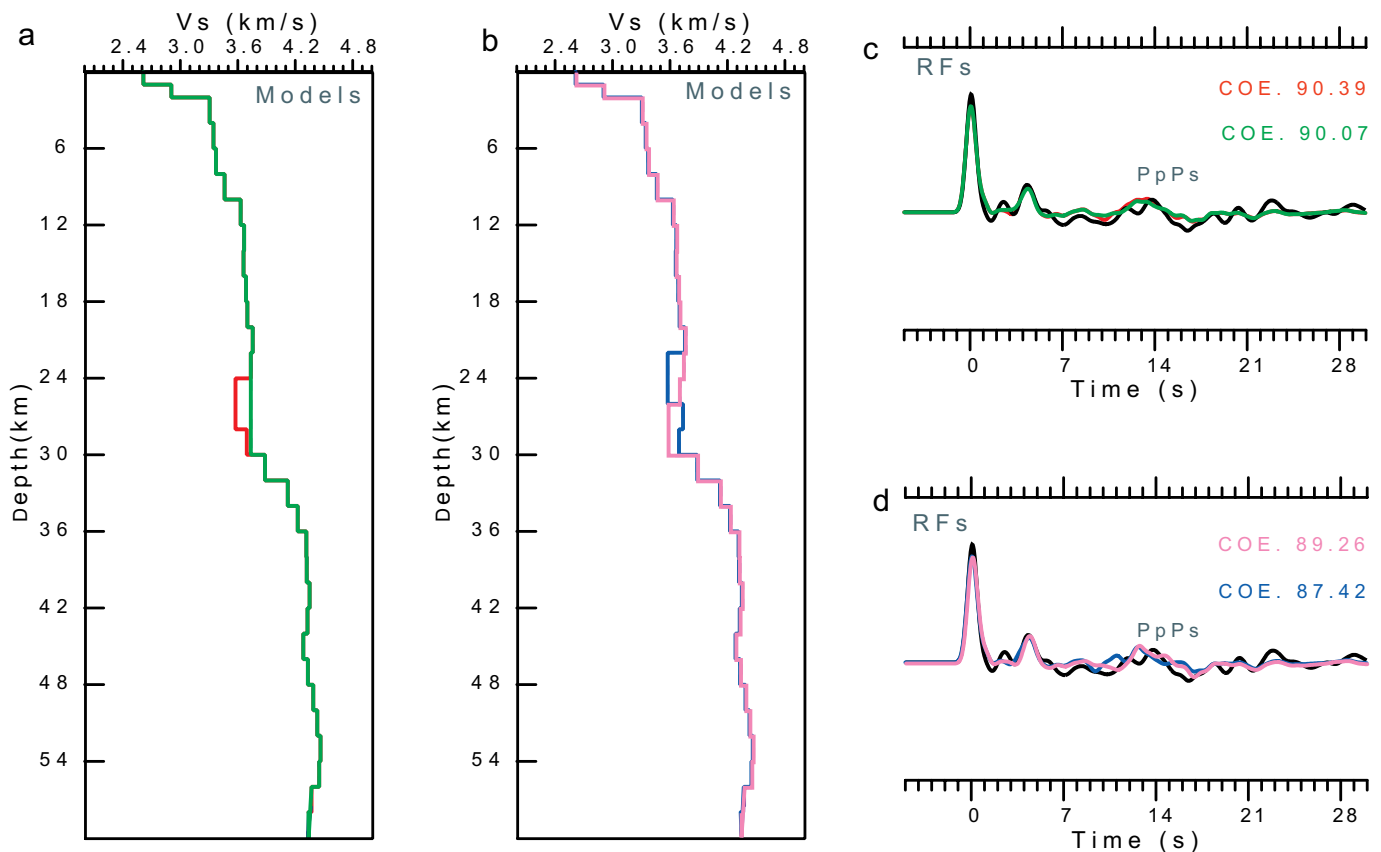


Fig. 11. Different S-wave velocities (a, b) and corresponding synthetic RFs (c, d) and real data (black lines in c, d) with a Gaussian factor of 2.0 for the station SDTCH. The coefficient of error (COE) shows the fitting degree between the synthetic and real RFs. (For interpretation of the references to color in this figure, the reader is referred to the web version of this article.)

CRedit authorship contribution statement

Zigen Wei: Investigation, Writing - original draft, Software.
Risheng Chu: Conceptualization, Writing - review & editing.
Ling Chen: Writing - review & editing, Resources.
Shanshan Wu: Investigation, Data curation.

Declaration of competing interest

The authors declare that they have no known competing financial interests or personal relationships that could have appeared to influence the work reported in this paper.

Acknowledgments

We are thankful to the State Key Laboratory of Geodesy and Earth's Dynamics (Institute of Geodesy and Geophysics, Chinese Academy of Sciences), the Seismic Array Laboratory, Institute of Geology and Geophysics, Chinese Academy of Sciences (doi:10.12129/IGGSL.Data.Observation, <http://www.seislab.cn/>) and Data Management Centre of China National Seismic Network at Institute of Geophysics (SEISDMC, doi:10.11998/SeisDmc/SN), China Earthquake Administration, for providing seismic data of temporary and permanent stations, respectively. We thank Huajian Yao and Weisen Shen to provide the phase velocity dispersion curves. We also thank Editor and two anonymous reviewers for their constructive reviews. This work is supported by the DREAM project of the National Key R&D Program of China (2016YFC0600402) and the National Natural Science Foundation of China (Grants 41604056).

References

- Chen, L., Zheng, T.Y., Xu, W.W., 2006. A thinned lithospheric image of the Tanlu Fault Zone, eastern China: constructed from wave equation based receiver function migration. *J. Geophys. Res.* 111, B09312. <https://doi.org/10.1029/2005JB003974>.
- Christensen, N.I., 1996. Poisson's ratio and crustal seismology. *J. Geophys. Res.* 101, 3139–3156.
- Deng, Q.D., Zhang, P.Z., Ran, Y.K., Yang, X.P., Min, W., Chu, Q.Z., 2003. Basic characteristics of active tectonics of China. *Sci. China Ser. D Earth Sci.* 46 (4), 356–372.
- Duan, Y.H., Wang, F.Y., Zhang, X.K., Lin, J.Y., Liu, Z., Liu, B.F., Yang, Z.X., Guo, W.B., Wei, Y.H., 2016. Three dimensional crustal velocity structure model of the middle-eastern North China Craton (HBCrust1.0). *Sci. China Earth Sci.* 59, 1477–1488.
- Gao, W.M., Zheng, L.S., Li, J.L., 1998. Seismogenic structure of the Tancheng 8.5 Ms in 1668. *Earthquake Research In China* 4 (3), 9–16 (in Chinese).
- Gu, Q.P., Ding, Z.F., Kang, Q.Q., Zhao, Q.G., 2016. Pn wave velocity and anisotropy in the middle-southern segment of the Tan-Lu fault zone and adjacent region. *Chin. J. Geophys.* 59 (2), 504–515 (in Chinese).
- He, R.Z., Shang, X.F., Yu, C.Q., Zhang, H.J., Van der Hilst, R., 2014. A unified map of Moho depth and Vp/Vs ratio of continental China by receiver function analysis. *Geophys. J. Int.* 199, 1910–1918.
- Herrmann, R.B., 2013. Computer programs in seismology, an evolving tool for instruction and research. *Seismol. Res. Lett.* 84 (6), 1081–1088.
- Hu, J.F., Zhu, X.G., Xia, J.Y., Chen, Y., 2005. Using surface wave and receiver function to jointly inverse the crust-mantle velocity structure in the West Yunnan area. *Chin. J. Geophys.* 48 (5), 1148–1155 (in Chinese).
- Huang, Z.X., Li, H.Y., Zheng, Y.J., Zheng, Y.J., Peng, Y.J., 2009. The lithosphere of North China Craton from surface wave tomography. *Earth Planet. Sci. Lett.* 288 (1–2), 173.
- Ji, S.C., Wang, Q., Salisbury, M.H., 2009. Composition and tectonic evolution of the Chinese continental crust constrained by Poisson's ratio. *Tectonophysics* 463, 15–30.
- Julià, J., Ammon, C.J., Herrmann, R.B., Correig, A.M., 2000. Joint inversion of receiver function and surface wave dispersion observations. *Geophys. J. R. Astron. Soc.* 143 (1), 99–112.
- Kennett, B.L.N., Engdahl, E.R., Buland, R., 1995. Constraints on seismic velocities in the earth from travel times. *Geophys. J. Int.* 122, 108–124.
- Li, Z.X., 1994. Collision between the north and south blocks: a crust-detachment model for suturing in the region east of the Tan-Lu fault. *Geology* 22 (8), 739–742.
- Li, S.L., Mooney, W.D., Fan, J.C., 2006. Crustal structure of mainland China from deep seismic sounding data. *Tectonophysics* 420, 239–252.
- Li, X.L., Li, Z.W., Hao, T.Y., Wang, S., Xing, J., 2017. A multi-frequency receiver function

- inversion approach for crustal velocity structure. *Comput. Geosci.* 102 (C), 45–55.
- Li, K., Xu, X.W., Wei, L.M., Wang, Q.X., Shu, P., 2019. Evidence of long recurrence times and low slip rate along the 1668 Tancheng earthquake fault. *Chin. Sci. Bull.* 64. <https://doi.org/10.1360/N972018-00961> (in Chinese).
- Liu, C.Q., Zhu, Y.P., Li, H.D., Zhang, C. k., 1983. Lianyungang-Linyi-Sishui DSS profile and the deep structure background of the Linyi earthquake of Ms8.5 Earthquake, (3): 11–17 (in Chinese).
- Ma, L.F., 2002. Geological Atlas of China. Geological publishing house (in Chinese).
- Meng, Y.F., Yao, H.J., Wang, X.Z., Li, L.L., Feng, J.K., Hong, D.Q., Wang, X.L., 2019. Crustal velocity structure and deformation features in the central-southern segment of Tanlu fault zone and its adjacent area from ambient noise tomography. *Chin. J. Geophys.* 67 (2), 2490–2509 (in Chinese).
- Shen, W.S., Ritzwoller, M.H., Kang, D., Kim, Y.H., Lin, F.C., Ning, J.Y., Wang, W.T., Zheng, Y., Zhou, L.Q., 2016. A seismic reference model for the crust and uppermost mantle beneath China from surface wave dispersion. *Geophys. J. Int.* 206 (2), 954–979.
- Tang, X.G., Chen, Y.S., Tang, Z., 2006. Bouguer gravity study of middle section of Tanlu fault. *Acta Seismol. Sin.* 19 (6), 650–657.
- Teng, J.W., 2010. Ponder and research on the genesis and occurrence of strong earthquakes and the prediction of their place, time and intensity. *Chin. J. Geophys.* 53 (8), 1749–1766 (in Chinese).
- Wang, H.L., Geng, J., 1996. Discussion about focus parameters of Tancheng earthquake of Tancheng earthquake of Ms8.5 in 1668. *Journal of Seismology* (4), 27–33 (in Chinese).
- Wang, D.H., Zhang, J.F., Wang, X., Jiang, W.L., Tian, T., 2018. Analysis of aeromagnetic anomalies and deep structure of Jiangsu segment of Tan-Lu fault zone and its adjacent region. *Prog. Geophys.* 33 (4), 1419–1429 (in Chinese).
- Wei, Z.G., Chen, L., Li, Z.W., Ling, Y., Li, J., 2016a. Regional variation in Moho depth and Poisson's ratio beneath eastern China and its tectonic implications. *J. Asian Earth Sci.* 115, 308–320.
- Wei, Z.G., Chu, R.S., Chen, L., Chong, J.J., Li, Z.W., 2016b. Analysis of h-k stacking of receiver functions beneath crust with complex structure: taking the Anatolia plate as an example. *Chin. J. Geophys.* 59 (11), 4048–4062 (in Chinese).
- Wu, S.S., Jiang, M.M., He, Y.M., Zhao, L., Ai, Y.S., 2018. NW-SE structural contrast of shear wave velocity and radial anisotropy beneath the Hefei-Jinhua seismic profile derived from ambient noise tomography. *Chin. J. Geophys.* 61 (2), 584–592 (in Chinese).
- Xu, J.W., Zhu, G., Tong, W.X., Cui, K.R., Liu, Q., 1987. Formation and evolution of the Tancheng-Lujiang wrench fault system: a major shear system to the northern of the Pacific Ocean. *Tectonophysics* 134 (4), 273–310.
- Xu, P. F., Liu, F.T., Wang, Q. C., Cong, B.L., Chen, H., Sun, R.M., 2000. Seismic tomography beneath the Dabie-Sulu collision orogen-3D velocity structures of lithosphere. *Chinese J. Geophys.* 43(3), 377–385 (in Chinese).
- Yan, L.J., Zhu, G., Lin, S.Z., Zhao, T., 2014. Neotectonic activity and formation mechanism of the Yishu Fault Zone. *Sci. China Earth Sci.* 57 (4), 614–629.
- Yeck, W.L., Sheehan, A.F., Schulte, P.V., 2013. Sequential H-k stacking to obtain accurate crustal thicknesses beneath sedimentary basins. *Bull. Seismol. Soc. Am.* 103, 2142–2150.
- Yu, Y.Q., Song, J.G., Liu, K.H., Gao, S.S., 2015. Determining crustal structure beneath seismic stations overlying a low-velocity sedimentary layer using receiver functions. *J. Geophys. Res. Solid Earth* 120. <https://doi.org/10.1002/2014JB011610>.
- Zhang, B.X., Tang, Y.G., 1988. Crustal structural characteristics of Yishu Fault Zone. *China earthquake* 3, 22–28 (in Chinese).
- Zhang, J.H., Zhao, G.Z., Xiao, Q.B., Tang, J., 2010. Analysis of electric structure of the central Tan-Lu fault zone (Yi Shu fault zone, 36°N) and seismogenic condition. *Chin. J. Geophys.* 53 (3), 605–611 (in Chinese).
- Zhang, H.S., Gao, R., Tian, X.B., Teng, J.W., Li, Q.S., Ye, Z., Liu, Z., Si, S.K., 2015. Crustal S-wave velocity beneath the northeastern Tibetan plateau inferred from teleseismic P wave receiver functions. *Chin. J. Geophys.* 58 (11), 3982–3992 (in Chinese).
- Zhao, L., Zheng, T.Y., Lv, G., 2013. Distinct upper mantle deformation of cratons in response to subduction, constraints from SKS wave splitting measurements in eastern China. *Gondwana Res.* 23, 39–53.
- Zheng, T. Y., Zhao, L., Xu, W. W., Zhu, R. X., 2008. Insight into modification of North China Craton from seismological study in the Shandong Province. *Geophysical Research Letters*, 35 (22). L22305, doi:<https://doi.org/10.1029/2008GL035661>.
- Zheng, X., Yao, Z., Liang, J., Zheng, J., 2010. The role played and opportunities provided by IGP DMC of China National Seismic Network in Wenchuan earthquake disaster relief and researches. *Bull. Seismol. Soc. Am.* 100 (5B), 2866–2872.
- Zheng, Y., Shen, W.S., Zhou, L.Q., Yang, Y.J., Xie, Z.J., Ritzwoller, M.H., 2011. Crust and uppermost mantle beneath the North China Craton, northeastern China, and the Sea of Japan from ambient noise tomography. *J. Geophys. Res.* 116, B12312. <https://doi.org/10.1029/2011JB008637>.
- Zhu, L.P., Kanamori, H., 2000. Moho depth variation in southern California from teleseismic receiver functions. *J. Geophys. Res.* 105, 2969–2980.
- Zhu, A.L., Xu, X.W., Wang, P., Ren, Y., Sun, D.J., 2018a. The present activity of the central and southern segments of the Tancheng-Lujiang fault zone evidenced from relocated microseismicity and focal mechanisms. *Earth Sci. Front.* 25 (1), 218–226 (in Chinese).
- Zhu, G., Liu, C., Gu, C.C., Zhang, S., Li, Y.J., Su, N., Xiao, S.Y., 2018b. Oceanic plate subduction history in the western Pacific Ocean: constraint from late Mesozoic evolution of the Tan-Lu Fault Zone. *Sci. China Earth Sci.* 61, 386–405.